Measurement report: Production and loss of atmospheric formaldehyde at a suburban site of Shanghai in summertime

Yizhen Wu[1], Juntao Huo[2], Gan Yang[1], Yuwei Wang[1], Lihong Wang[1], Shijian Wu[2], Lei Yao[1], Qingyan Fu[2], Lin Wang[1,3,4,5,6]

[1] Shanghai Key Laboratory of Atmospheric Particle Pollution and Prevention (LAP[3]), Department of Environmental Science & Engineering, Jiangwan Campus, Fudan University, Shanghai 200438, China

[2] Shanghai Environmental Monitoring Center, Shanghai 200030, China

[3] Collaborative Innovation Center of Climate Change, Nanjing, 210023, China

[4] Shanghai Institute of Pollution Control and Ecological Security, Shanghai 200092, China

[5] IRDR International Center of Excellence on Risk Interconnectivity and Governance on Weather/Climate Extremes Impact and Public Health, Fudan University

[6] National Observations and Research Station for Wetland Ecosystems of the Yangtze Estuary, Shanghai, China

Correspondence to: Qingyan Fu (qingyanf@sheemc.cn) and Lin Wang (lin_wang@fudan.edu.cn)

Abstract. Formaldehyde (HCHO) is an important trace gas that affects the abundance of HO_2 radicals and ozone, leads to complex photochemical processes, and yields a variety of secondary atmospheric pollutants. In a 2021 summer campaign at the Dianshan Lake (DSL) Air Quality Monitoring Supersite in a suburban area of Shanghai, China, we measured atmospheric formaldehyde (HCHO) by a commercial Aero-Laser formaldehyde monitor, methane, and a range of non-methane hydrocarbons (NMHCs). Ambient HCHO showed a significant diurnal cycle with an average concentration of 2.2±1.8 ppbv (parts per billion by volume). During the time period with the most intensive photochemistry (10:00-16:00 LT), secondary production of HCHO was estimated to account for approximately 69.6% according to a multi-linear regression method based on ambient measurements on HCHO, acetylene (C_2H_2), and ozone (O_3). Average secondary HCHO production rate was estimated to be 0.73 ppbv h^{-1} during the whole campaign (including daytime and nighttime), with a dominant contribution from reactions between alkenes and OH radicals (66.3%), followed by OH radical-initiated reactions with alkanes and aromatics (together 19.0%), OH radical-initiated reactions with OVOCs (8.7%), and ozonolysis of alkenes (6.0%). An overall HCHO loss, including HCHO photolysis, reactions with OH radicals, and dry deposition, was estimated to be 0.49 ppbv h^{-1}. Calculated net HCHO production rates were in relatively good agreements with the observed rates of HCHO concentration change throughout the sunny days, indicating that HCHO was approximately produced by oxidation of the 24 hydrocarbons we took into account at the DSL site during the campaign, whereas calculated net HCHO production rates prevailed over the observed rates of HCHO concentration change in the morning/midday hours in the cloudy and rainy days, indicating a missing loss term, most likely due to HCHO wet deposition. Our results suggest the important role of secondary pollution at the suburb of Shanghai, where alkenes are likely key precursors for HCHO.

1 Introduction

Formaldehyde (HCHO) is the most abundant carbonyl in the troposphere, which is an intermediate product from the oxidation of various volatile organic compounds (VOCs) and plays an important role in various photochemical processes as both a source and a sink of free radicals (Wittrock et al., 2006). Photolysis of HCHO produces HO_2 radicals that can be subsequently converted to OH radicals, altering the oxidative capacity of the atmosphere (Mahajan et al., 2010; Tan et al., 2019a). HCHO can also contribute to ozone (O_3) formation, and their link is one of the most popular topics of atmospheric research (Hong et al., 2022; Liu et al., 2007; Pavel et al., 2021). Furthermore, HCHO can play a crucial catalytic role in the formation of particulate matters via in-cloud processing pathways to form hydroxymethyl hydroperoxide (HMHP) or hydroxymethanesulfonate (HMS) (Dovrou et al., 2022). Besides, HCHO has adverse health effects on humans and animals, possibly causing respiratory and cardiovascular diseases (Zhu et al., 2017).

Direct emission of HCHO can be attributed to anthropogenic activities, such as vehicle exhaust, industrial emissions, and fossil fuel combustion, and thus primary HCHO is closely related to anthropogenic pollutants such as acetylene (C_2H_2), carbon monoxide (CO), nitrogen oxidizes (NO_x) and traffic-related black carbon (BC) (de Gouw et al., 2005; Zhang et al., 2013; Dutta et al., 2010; Possanzini et al., 2002; Lin et al., 2012). Observations in city centers usually showed important HCHO sources of direct anthropogenic emissions (Dutta et al., 2010; Possanzini et al., 2002; Lin et al., 2012). On the other hand, previous studies indicate that secondary production of HCHO plays an important role in remote areas, which comes from complex oxidation processes of a wide range of VOCs by ubiquitous atmospheric oxidants like OH radicals and O_3 (Lin et al., 2012; Anderson et al., 2017; Nussbaumer et al., 2021). Especially in summertime, increases in temperature are always linked with higher solar radiation and larger biogenic isoprene emission, which have been proved to jointly contribute to the higher abundance of HCHO (Choi et al., 2010; Sumner et al., 2001; Wang et al., 2017). Due to the short lifetime of HCHO, primary emissions and transport processes are important in source regions but can be mostly neglected in remote locations. On the other hand, secondary HCHO production paths are more diverse and complex, and thus they are difficult to be quantified.

In previous studies, several methods were used to separate the primary and secondary sources of HCHO, including the emission ratios of HCHO-to-tracers from primary sources (Possanzini et al., 2002; Lin et al., 2012), the photochemical age-based parameterization (de Gouw et al., 2005, 2018; Wang et al., 2017), receptor models such as the positive matrix factorization (PMF) model and the principal component analysis (PCA) model (Wang et al., 2017; Chen et al., 2014), and the multi-linear regression method based on ambient measurements of HCHO and various tracers that can represent primary and secondary sources, respectively (Su et al., 2019; Zhang et al., 2021b). These methods just provide a simple estimation on the ratios of different HCHO sources. Nevertheless, contributions of different precursors are the key to understand and prevent HCHO production, but a qualitative and quantitative understanding on the HCHO production and loss is still incomplete.

HCHO sources have been previously studied in China (Xing et al., 2020; Su et al., 2019; Wang et al., 2017; Sun et al., 2021; Zhang et al., 2021b), in which general fractions of primary and secondary HCHO were provided and important roles of secondary HCHO sources were suggested. Primary and secondary contributions to ambient HCHO were separated using a

65   multiple linear regression based on HCHO observed by Ozone Mapping and Profiler Suite (OMPS) in the Yangtze River Delta in China, suggesting that secondary formation, especially photochemical production, played crucial roles (Su et al., 2019; Zhang et al., 2021b). A more recent study used the GEOS-Chem model to stimulate the concentrations of HCHO over Hefei Province in summer, indicating that oxidations of both methane and nonmethane VOCs dominated the HCHO production with a contribution of 43.27% and 56.73%, respectively (Sun et al., 2021). To the best of our knowledge, little has been done to

70   quantify the contributions of various specific precursors to HCHO production in China.

On the other hand, studies that have estimated the secondary HCHO production and discriminated the contribution of different secondary HCHO precursors in North America and Europe still found missing production terms (Lin et al., 2012; Sumner et al., 2001). For example, missing HCHO production rates of 1.1-1.6 ppbv h^{-1} were reported for a remote site in America, which was nearly double of the calculated secondary production rates (Choi et al., 2010). Moreover, very few studies

75   have evaluated the HCHO budget by comparing the net production of HCHO (P(HCHO)-L(HCHO)) and the observed rates of HCHO concentration change, and even for those with such attempts, discrepancies remained (Sumner et al., 2001; Zhang et al., 2021a). Therefore, an estimation of secondary HCHO production based on a comprehensive observation of HCHO precursors, as well as a comprehensive understanding on the formation and loss of HCHO to fill the gap in the HCHO budget calculation, is urgently needed to reveal the key precursors to HCHO formation, especially in eastern China where

80   photochemical pollution is getting severe in recent years.

In this study, we measured atmospheric HCHO concentrations, using a commercial Aero-Laser formaldehyde monitor, from June 10 to July 4, 2021 at the Dianshan Lake (DSL) Air Quality Monitoring Supersite, a suburban area of Shanghai. The secondary HCHO production rates were estimated based on parallel measurements of O$_3$, photolysis frequencies, and 24 VOCs whose photochemical reactions lead to formation of HCHO. The loss of HCHO including HCHO photolysis, reactions with

85   OH radicals, and dry deposition was estimated. Also, characteristics of secondary HCHO production between the sunny period and the cloudy and rainy period were compared. Lastly, the calculated net HCHO production rates were compared with the observed rates of HCHO concentration change.

2 Methodology

2.1 Measurement site

90   A comprehensive campaign was carried out at the DSL Air Quality Monitoring Supersite in Shanghai, China (31.10°N, 120.98°E), covering June 10 to July 4, 2021. The station is located in Qingpu District in the western suburb of Shanghai, which is about 37 km away from the city center, and surrounded by Dianshan Lake and several villages with a small quantity of residents (Figure 1). There is a highroad (G318) about 0.4 km southeast of the sampling site. Since it is located at the junction of Shanghai, Zhejiang Province and Jiangsu Province, all of which are well developed areas with large populations, this super
95   site is often affected by regional transport and suffers from photochemical pollution episodes (Yang et al., 2022).

2.2 Measurements of VOCs

Atmospheric HCHO was measured by a commercial Aero-Laser formaldehyde monitor (Aerolaser GmbH., model AL4021) with a detection limit (DL) of 100 pptv (parts per trillion by volume). In this instrument, gaseous HCHO is firstly absorbed by sulfuric acid (0.3%) and transferred into liquid phase, and then the aqueous HCHO reacts with acetylacetone and ammonia to
100   produce 3,5-diacetyl-1,4-dihydrolutidine (DDL), which can be excited by a laser at 410 nm and the fluorescence at 510 nm is used to quantify HCHO. Liquid formaldehyde standards of 80 μg L^{-1} were used to calibrate the instrument weekly. HCHO was measured at a time resolution of 5 min but the obtained data was processed to those at 1 hr intervals to match the VOC data from an online gas chromatograph equipped with mass spectrometry and flame ionization detection (GC-MS/FID).

Atmospheric methane was measured with GC-FID (ChromaTHC, model C24022). Methane was separated from ambient
105   non-methane hydrocarbons (NMHCs), since NMHCs were concentrated in a packed stainless-steel column filled with Porapak Q, 50/80 Mesh, whereas methane was able to freely pass the column and to be detected by a hydrogen ion flame detector. Methane standards of 2 ppmv (parts per million by volume) were used to perform instrument calibration every week, and those at five concentration levels (0, 1, 2, 3, 4 ppmv) were used to quantify the concentration of ambient methane. The concentration of methane was detected at a time resolution of 5 min but averaged to those at 1 hr intervals to match the GC-MS/FID data.
110   Sampling Measurements of Photochemical Assessment Monitoring Station (PAMS) VOC compounds were performed for 10 min each hour, and the resulting data from with GC-MS/FID (TH-PKU 300B) analysis were used to represent concentrations of PAMS compounds in that hour with a time resolution of 1 hour, given the time for heating and cooling of the GC oven (Li et al., 2015). This practice may miss spikes of PAMS concentration variation, but on a longer time scale, the general characteristics of ambient air composition and concentrations likely still show similar features in one hour (Kumar and Sinha,
115   2014; Li et al., 2015; Yuan et al., 2012; Yang et al., 2022). Ambient concentrations of 2-methyl pentane were always below the detection limit of this compound in the instrument, and thus the corresponding data was not included. Ambient air was

sampled into the system, where C2-C5 hydrocarbons were separated by a Porous Layer Open Tubular column (PLOT) (Agilent Technologies Inc.) and measured by the FID channel, and the other hydrocarbons (C6-C12) were preconcentrated by a semi-polar column (DB-624, Agilent Technologies Inc.) and detected using a quadrupole MS detector. Weekly calibration was conducted by a built-in auto-calibration system, using gaseous bromochloromethane, 1,2-difluorobenzene, chlorobenzene-d5, and bromofluorobenzene in high purity N_2, each of which is of 4 ppbv. Mixtures of 57 PAMS compounds at five concentration levels (0, 1, 2, 4, 8 ppbv) were used to quantify the ambient concentrations of these species.

Isoprene, alpha-pinene, methyl vinyl ketone (MVK) and methacrolein (MACR) were detected by a two-channel gas chromatograph with electron ionization time-of-flight mass spectrometer (GC-EI-TOF-MS) system. The GC-EI-TOF-MS system consists of three main components: (1) a thermal desorption pre-concentrator (TDPC) (Aerodyne Research Inc.) for sample collection, (2) a gas chromatograph (GC) (Aerodyne Research Inc.) for sample separation, and (3) an electron ionization time-of-flight mass spectrometer (EI-TOF-MS) (Tofwerk AG, model EI-HTOF) for sample detection (Obersteiner et al., 2016; Claflin et al., 2021). Before pre-concentration, the ambient sample is passed through a bed of pre-cleaned sodium sulfite (nominal 1g) held in a quartz tube with glass wool packing to scrub ozone and thereby reduce sampling artifacts (Helmig, 1997). The TDPC employed for this campaign relied upon two-stage adsorbent traping for preconcentration of analytes, using multibed, preconditioned glass sample tubes (1/4" OD; Markes International), followed by sample focusing on narrow-bore, multibed glass focus traps (1/8" OD, Markes International). The first stage of trapping allows sampling rates up to 100 sccm, followed by a post-collection purge with dry gas to remove water before focusing; during this campaign, the sample volume was about 800 cm^3 per channel. The ARI GC was configured as a two-channel system to expand the volatility range, with a 30 m Rxi-624 analytical column (Restek, 0.25 mm ID, 1.4 μm film thickness) for Channel 1 and a 30 m MXT-WAX analytical column (Restek, 0.25 mm ID, 0.25 μm film thickness) for Channel 2. Isoprene, alpha-pinene, MVK and MACR were all analyzed on the Rxi-624 column, which ran a ramped temperature program optimized for C5-C12 hydrocarbons, along with oxygen-, nitrogen-, halogen-, and sulfur-containing VOCs. Automated gas-phase calibration and instrument background of GC-EI-TOF-MS was conducted every 20 hours with a standard gas cylinder (Apel-Riemer Environmental Inc.), including MVK, furan, propanal, methyl tert-butyl ether, butanal, ethyl acetate, toluene, octane, m-xylene, o-xylene, naphthalene, 1-methylnaphthalene, decamethylcyclopentasiloxane, and limonene. MVK was calibrated during the campaign with the automated gas-phase calibration as mentioned above. Isoprene and alpha-pinene were calibrated after the campaign using another calibrant cylinder (Weichuang Standard Reference Gas Analytical Technology Co., Ltd.), where a 5-point calibration was conducted and each point was repeated for 3 times. As for MACR, calibration was conducted after the campaign with a liquid calibration system (LCS, Tofwerk AG). Briefly, liquid MACR was diluted with methanol, and injected steadily into a stream of 2 slpm (standard liters per minute) ultra-high-purity N_2 with a high precision syringe pump, part of which (around

198 sccm) was guided into the GC-EI-TOF-MS. The sampling time of GC-EI-TOF-MS was adjusted to obtain a 4-point calibration curve with 3 duplicates for each point. The consistency between the liquid calibration and the calibrant cylinder calibration was confirmed by conducting both calibration methods for m-xylene, o-xylene, 1,2,4-TMB, and benzene. The sensitivity of the GC-EI-TOF-MS during and after the campaign was calibrated and normalized using the first standard gas cylinder (Apel-Riemer Environmental Inc.). Concentrations of isoprene, alpha-pinene, MVK and MACR were measured with a time resolution of 30 min, which were later averaged into those at 1 hr intervals to match the GC-MS/FID data.

Isoprene was detected by both GC-MS/FID (DL of 0.04 ppbv for isoprene) and GC-EI-TOF-MS (DL of 0.77 pptv), and the corresponding inter-comparison is shown in Figure S1. Daytime isoprene concentrations showed excellent agreements between two systems (Figure S1a), whereas at nighttime, GC-MS/FID usually showed higher results than GC-EI-TOF-MS when concentrations of isoprene declined to low values, as shown in Figure S1b. The reason for the discrepancy at night is unknown. Considering the lower detection limit and higher accuracy of GC-EI-TOF-MS, isoprene measured by GC-EI-TOF-MS will be used in the following discussion. The good correlation between daytime isoprene concentrations suggests minor uncertainties of our daytime isoprene concentrations. Though there was a discrepancy between nighttime isoprene concentrations, the concentrations of measured isoprene and estimated OH radicals at night were so low that they hardly affect our results of calculated secondary HCHO production rates.

2.3 Measurements of other pollutants and meteorological parameters

O_3 was measured with an ultraviolet photometric analyzer (Thermo Environmental Instruments, TEI Inc., Model 49i) with a DL of 1 ppbv (at a time interval of 10 s). NO and NO_2 mixing ratios were determined using a chemiluminescent analyzer (TEI, Model 42i), DL for which is 0.40 ppbv (at a time interval of 60 s).

Photolysis frequencies of HCHO, NO_2, NO_3, O^1D, HONO, H_2O_2 were determined with an Ultra-fast CCD-Detector Spectrometer (Metcon, UF-CCD), with a time resolution of 1 min. The instrument consists of an optical receiver, a Charge-Coupled detector (CCD) and a cooling control box for the detector, and covers spectral band range from 280-650 nm. The photolysis frequencies can be calculated automatically from the measured spectra and the calibration factor, which is obtained from the calibration using NIST/PTB 1000W halogen lamps.

Temperature (T), relative humidity (RH), atmospheric pressure (P), wind speed (WS), wind direction (WD) and rainfall were captured by an automatic and commercial weather monitoring station (Vaisala AWS310). Boundary layer height (BLH) was recorded by a ceilometer (Vaisala, CL31). Atmospheric parameters were measured at a time resolution of 5 min.

All trace gases, meteorological parameters and photolysis frequencies were then processed to those at 1 hr intervals to match the GC-MS/FID data.

More details about the detection limit and accuracy of trace gases, VOCs, photolysis frequencies and BLH can be found in Table S2. Total uncertainties of calculated HCHO production and loss rates were estimated by applying the root square propagation of corresponding uncertainties of quantities used for the calculation.

3 Results

3.1 Overview of the campaign

This campaign was carried out from June 10 to July 4, 2021 at the DSL site. The sampling period coincided with the Plum Rain Season, a typical east Asian rainy period that features several weeks of wet days as well as high temperatures and usually starts in June, causing a significant weather variation during the campaign.

Figure 2 shows the time profiles of HCHO, O_x (=NO_2+O_3), O_3, NO_x, photolysis frequencies of O^1D ($J(O^1D)$) and meteorological parameters during the campaign. Datapoints are sometimes missing in the case of instrument routine calibrations and a couple of instrument failure. In addition, Table S1 summarizes the averages and the 10th and 90th percentiles of O_3, NO, NO_2, C_2H_2, wind speed, temperature, and relative humidity for the entire campaign, and $J(O^1D)$, $J(HCHO\_M)$, and $J(HCHO\_R)$ from sunrise to sunset during the campaign.

$J(O^1D)$ showed a normal diurnal variation, the daytime $J(O^1D)$ from sunrise to sunset is characterized with an average of 1.23×10^{-5} s^{-1} and a 10th and 90th percentile of 1.24×10^{-6} s^{-1} and 3.08×10^{-5} s^{-1}, respectively. Ambient temperature was characterized with an average of 26 °C and a 10th-90th percentile range of 23-30 °C, and RH showed an average of 83% and a 10th-90th percentile range of 62-98%, which is consistent with the typical features of the Plum Rain Season. The prevailing winds were from southeast, with an average speed of 1.8 m s^{-1}.

The concentration of O_3 was characterized with an average of 31 ppbv and varied in a 10th-90th percentile range of 8-59 ppbv. The 10th-90th percentile concentrations of NO and NO_2 were 2-8 and 7-23 ppbv, with average values of 6 and 14 ppbv, respectively. The daily maximum 1 h-O_3 concentration of five days during the campaign have exceeded Class I of China National Air Quality Standards (CNAAQS), i.e., an hourly average of 160 μg m^{-3} (~75 ppbv). Compared with a previous campaign operated at the DSL site in the summer of 2020, where the average concentrations of O_3, NO, and NO_2 were 37 ppbv, 4 ppbv, and 18 ppbv, respectively (Yang et al., 2022), the concentrations of these pollutants in this observation were similar.

HCHO mixing ratios ranged up to the maximum of 9.4 ppbv, with the average value of 2.2±1.8 ppbv (one standard deviation) and the median value of 1.8 ppbv. This value was comparable to that (2.2 ppbv) reported in the urban area of New York (USA) in summertime (Lin et al., 2012), but lower than those (5.07 and 5.0 ppbv, respectively) observed in the urban area of Shanghai (China) and Shenzhen (China) (Ho et al., 2015; Wang et al., 2017). However, the HCHO concentration level at the DSL site

was higher than those (1.5, 1.34, 1.1, 1.1, and 0.4 ppbv, respectively) reported in remote areas in Mazhuang Town (China), Whiteface Mountain (USA), Ineia (Cyprus), Hohenpeißenberg (Germany) and Hyytiälä (Finland) (Wang et al., 2010; Zhou et al., 2007; Nussbaumer et al., 2021).

In Figure 2, O_3 and O_x showed relatively high abundances while the concentration of traffic-related species like NO_x was low. This hints that HCHO at the observation site was potentially associated more with the secondary sources. Figure 3a further illustrates the diurnal variations of HCHO, O_3 and C_2H_2 at the DSL site during the campaign. Both HCHO and O_3 exhibited strong diurnal variations during the field measurement, which reached the maximum in the early afternoon, decreased gradually in the afternoon, and remained flat at night. The good correlation between hourly concentrations of HCHO and O_3 (R^2=0.73), as shown in Figure 3b, indicates important contributions of secondary sources to HCHO. By contrast, the variations of HCHO and C_2H_2 in Figure 3a are less parallel. C_2H_2 increased in the early morning since around 5:00 LT (local time), reached its maximum in the rush hours at 8:00-9:00 LT, then decreased till noon, and remained relatively steady with a much smaller peak in the evening around 20:00 LT, which likely coincided with the traffic volumes on the highroad. The correlation (R^2=0.55) between HCHO and C_2H_2 was lower compared to the correlation between HCHO and O_3, as shown in Figure 3c. These observations roughly indicate that HCHO at the DSL site was more influenced by secondary sources than primary sources.

Here, we present a multi-linear regression method based on measurements on ambient HCHO, C_2H_2, and O_3 to estimate contributions of background, primary, and secondary HCHO. C_2H_2 is used here as an indicator of primary emissions, whereas O_3 is used as a tracer of secondary production. A linear regression model was used to establish a link among the time series of HCHO, C_2H_2, and O_3 (Garcia et al., 2006; Zhang et al., 2021b; Su et al., 2019; Sun et al., 2021). The observed HCHO can be reproduced by the following linear regression model as shown in Eq. (1).

$$[HCHO] = \beta_0 + \beta_1[C_2H_2] + \beta_2[O_3] \tag{1}$$

where β_0, β_1, and β_2 are the fitting coefficients calculated from the multiple linear regression, and [HCHO], $[C_2H_2]$ and $[O_3]$ represent the concentrations of HCHO, C_2H_2 and O_3, respectively. The relative contributions of background , primary , and secondary sources to ambient HCHO can be calculated using Eq. (2)- Eq. (4) (Garcia et al., 2006; Zhang et al., 2021b; Su et al., 2019; Sun et al., 2021).

$$R_{Background} = \frac{\beta_0}{\beta_0 + \beta_1[C_2H_2] + \beta_2[O_3]} \tag{2}$$

$$R_{Primary} = \frac{\beta_1[C_2H_2]}{\beta_0 + \beta_1[C_2H_2] + \beta_2[O_3]} \tag{3}$$

$$R_{Secondary} = \frac{\beta_2[O_3]}{\beta_0 + \beta_1[C_2H_2] + \beta_2[O_3]} \tag{4}$$

where $R_{Primary}$ denotes the relative contribution of HCHO from primary sources, $R_{Secondary}$ represents the relative contribution of HCHO from secondary sources, and $R_{Background}$ denotes the relative contribution of background HCHO,

which may come from alternated HCHO sources with different residence times or transport of HCHO into the airshed and cannot be classified as primary or secondary sources.

Figure 4 reveals the time series of and percentile contributions of background, primary, and secondary HCHO. The modelled HCHO and measured HCHO show a significant linear regression (R=0.86) (Figure 4a), which confirms that the multiple linear regression model is statistically reliable. Secondary HCHO dominated local HCHO during the daytime, whereas primary HCHO was more important during nighttime and in the early morning, when photochemical reactions could be nearly neglected (Figure 4b). The campaign-average relative contributions of secondary production (Figure 4c) showed the lowest value at 5:00 LT, which was associated with weaker photochemical reactions and higher vehicle emissions due to the morning rush hours. After that, with the increasingly active photochemistry, percentages of secondary HCHO started to rise and reached the peak in the early afternoon (around 13:00-15:00 LT), and then gradually decreased. On average, background, primary, and secondary HCHO contributed 12.7%, 30.4%, and 56.9% to ambient HCHO during the campaign, whereas during the time period with the most intensive photochemistry (10:00-16:00 LT), their relative contributions were 9.5%, 20.9%, and 69.6%, respectively.

Another simple method of separating the primary HCHO and secondary HCHO is shown in the Supplement (Sect. S1) for comparison. Diurnal variations of relative contributions of secondary HCHO from two methods are quite similar, as shown in Figure S2 and Figure 4, though there are tiny differences between the absolute numbers, e.g., 65.7% according to the ratios of HCHO/C_2H_2 and 69.6% from the multi-linear regression method, respectively. The estimated contributions of secondary HCHO indicate an important role of secondary HCHO production, especially during the daytime, when the photochemistry is more active.

3.2 HCHO production from VOC oxidation

HCHO is secondarily produced through oxidation of a wide range of atmospheric VOCs by oxidants including OH and O_3. Hence, with HCHO yields reported in literatures for these oxidation processes and the concentrations of the parent VOCs and oxidants, the chemical production rate of HCHO can be estimated as shown in Eq. (5) (Lee et al., 1998; Sumner et al., 2001; Choi et al., 2010; Lin et al., 2012).

$$P(HCHO) = \sum_i \sum_j \left(\gamma_{ij} k_{ij} [VOC]_j [Oxindant]_i \right) \tag{5}$$

where i denotes the ith kind of oxidant such as OH or O_3, j denotes the jth VOC species that produces HCHO through its oxidation, and k_{ij} and γ_{ij} represent the reaction rate coefficient and the corresponding HCHO yield for the reaction between the ith oxidant and the jth VOC, respectively.

Over 60 VOC species were detected during the campaign, but only 24 VOC species whose oxidation will produce HCHO were used in the calculation of HCHO production rates, including 12 alkanes, 1 aromatic, 9 alkenes and 2 OVOCs.

Concentrations of theses 24 VOCs are summarized in Table S3, and the corresponding reaction rate coefficients and HCHO yields taken in the calculation are described in Table S4. The VOC species considered are quite comprehensive, though acetaldehyde, methanol, and methylhydrogenperoxide (MHP) are not available in this study. These three compounds, together with acetone, were estimated to contribute up to 7% to secondary HCHO formation at the DSL site, using their concentrations reported in previous studies and that for acetone in our study (Yang et al., 2022; Han et al., 2019; Yuan et al., 2013; Zhang et al., 2012; Nussbaumer et al., 2021). Therefore, we consider their absence would not influence our results considerably.

There was not a direct measurement of OH radical concentrations during this campaign, and thus we adopted an empirical equation that has been suggested for OH concentration estimations in four Chinese megacities including Shanghai, as shown in Eq. (6) (Liu et al., 2020; Tan et al., 2019a; Fan et al., 2021),

$$[OH] = J(O^1D) \times 3 \times 10^{11} \; molecules \; cm^{-3} \qquad (6)$$

where $J(O^1D)$ denotes photolysis frequencies of O^1D. We compared our calculation results (Table S5) with those from another recommendation (Sect. S2) (Ehhalt and Rohrer, 2000), and their good correlation (R=0.97) and a slope close to 1 in Figure S3 validates our estimates. The uncertainties of OH concentration from the calculation were estimated to be 20%, and this uncertainty was used to estimate those in the production rates and loss rates of HCHO (Tan et al., 2019a; Rohrer and Berresheim, 2006). Figure 5 presents the profile of the calculated HCHO production rates during the whole campaign with a time resolution of 1 hr. Overall, alkenes oxidation by OH radicals contributed the most to secondary HCHO production, accounting for 66.3%, followed by OH-radical initiated reactions with alkanes and aromatics (19.0%) and reactions of OVOCs (8.7%), while ozonolysis of alkenes contributed by 6.0%, which was the smallest contribution reaction pathway. The average of calculated secondary HCHO production rate was 0.73 ppbv h^{-1}, with a 90th percentile of 2.42 ppbv h^{-1} and a 10th percentile of 0.01 ppbv h^{-1}. Peaks of secondary HCHO production rates were usually observed at noon, and the rates showed obvious diurnal cycles. On the other hand, the rates varied significantly during the campaign because secondary HCHO production relies heavily on the weather condition, i.e., photochemical reactions are usually much more active in the sunny days than in the cloudy and rainy period. As we have mentioned before, there were obvious weather variations during the campaign. Therefore, we divided our campaign into the sunny period (including 12 days) and the cloudy and rainy period (13 days) for further investigation. Comparison of the secondary HCHO production between the sunny period and the cloudy and rainy period is shown in Table 1 and Figure 6.

In Figure 7, relative contributions to HCHO production from various processes during the sunny and the cloudy and rainy periods, respectively, are shown, together with the top 10 VOC species that contributed the most in each period, which in total yielded more than 90% of the overall HCHO. During the sunny days (Figure 7a), HCHO production was dominated by the reactions of alkenes and OH radicals, accounting for 64.8%, followed by OH radical-initiated reactions with alkanes and

aromatics (19.5%), OH radical-initiated reactions with OVOCs (10.4%), and ozonolysis of alkenes (5.3%). As the graph shows,

295   32.3% of the secondary HCHO production came from isoprene oxidation (by both OH radical and O_3), where OH oxidation

of isoprene (30.6%) overwhelmed. The other main contributors in the sunny days were associated with OH radical-initiated

reactions with ethene (19.4%), methane (12.9%), propene (10.6%), and MVK (8.0%), which together with isoprene

represented more than 80% of the overall HCHO production.

For the cloudy and rainy period (Figure 7b), the relative contribution to secondary HCHO from OH radical-initiated

300   reactions with alkenes increased a little, accounting for 68.3%, while OVOCs oxidation by OH radicals decreased to 5.8%.

MVK and MACR are known as the major intermediate products generated from isoprene oxidation. The less intensive solar

radiation in the cloudy and rainy days influences both the abundance and the oxidation processes of MVK and MACR to form

HCHO, leading to their declined fraction to HCHO production (Gong et al., 2018; Guo et al., 2012; Gu et al., 2022). Meanwhile,

the total contribution from isoprene oxidation decreased to 21.0% due to the combination of lower isoprene concentrations

305   and OH abundances. In the cloudy and rainy days, the dominant pathways to HCHO production were OH radical-initiated

reactions with ethene, isoprene, propene and methane, yielding 30.2%, 21.0%, 13.2% and 11.9%, respectively, of the total

HCHO production from VOCs we have measured.

For both the sunny period and the cloudy and rainy period, ethene and propene turned out to be two of the most important

precursors, but their significance has not been reported in previous studies, which might be attributed to the forest environments

310   where most previous studies were conducted (Choi et al., 2010; Sumner et al., 2001). Also, the importance of MVK and MACR

was not found previously, but these two precursors turned out to play an important role in secondary HCHO production in our

study. To the best of our knowledge, there is only one study that has previously calculated HCHO production from various

alkanes in an urban area in USA (Lin et al., 2012). Our study takes a wide range of VOCs including alkanes, alkenes, aromatic

and OVOCs into the calculation of HCHO production rates.

315   The average diurnal patterns of secondary HCHO production showed clear differences between the sunny and the cloudy

and rainy periods, as shown in Figure 8. During the sunny period (Figure 8a), HCHO production rates displayed a strong

diurnal cycle, with a peak of 3.80 ppbv h^{-1} observed at 13:00 LT when photochemical reactions were intense, and were roughly

constant at about 0.03 ppbv h^{-1} during nighttime (from 19:00 to 5:00 LT next day). During this low-rate period, about 98% of

the HCHO production came from ozonolysis of alkenes, since the estimated average nighttime concentration of OH radicals

320   was lower than 1500 molecules cm^{-3}, i.e., 5.58×10^{-5} pptv, while that of O_3 was still as high as 5.68×10^{11} molecules cm^{-3}, i.e.,

21.15 ppbv. After sunrise at 5:00 LT, HCHO production rates increased dramatically, reaching the maximum of 3.80 ppbv h^{-1}

at 13:00 LT, and then reduced until sunset at around 18:00 LT. Although O_3 concentration was higher than that of OH radicals

during the daytime, the rate constants for reactions of alkenes with O_3 are several orders of magnitude lower than those with OH, resulting in the dominant HCHO formation by alkenes oxidation with OH.

325 In the cloudy and rainy period (Figure 8b), nighttime HCHO production rates were almost equivalent to those in the sunny days, and also dominantly came from alkene ozonolysis. Secondary HCHO production rates began to rise after 5:00 LT, peaked at 10:00 LT (1.82 ppbv h^{-1}), maintained high (~1.69 ppbv h^{-1}) until 13:00 LT, and then started to fall to low values at night. This trend is consistent with the variation of the photolysis frequencies, which remained the highest values between 10:00-13:00 LT in the rainy and cloudy days, whereas they kept growing after sunrise and peaked at 13:00 LT in the sunny days.

330 The diurnal average HCHO production rates in the cloudy and rainy days (0.51 ppbv h^{-1}) were nearly half of the average in the sunny days (0.97 ppbv h^{-1}).

By applying the root square propagation of uncertainties in the reaction rate coefficients and corresponding HCHO yields for reactions between VOCs and oxidants, measurements of 24 VOCs and ozone, and estimations of OH (Table S6), the total uncertainties of the HCHO production rates were estimated to be 25.9% in the sunny period, and 21.0% in the cloudy and
335 rainy period.

3.3 HCHO sinks

Reactions (R1) — (R3) show the dominant daytime chemical loss processes of HCHO, i.e, direct oxidation by OH radicals, and two different photolysis pathways. The overall HCHO loss rate by photolysis can be calculated from measured HCHO concentration and its photolysis rate constants, J(HCHO_M) and J(HCHO_R) (shown in Table S1). These major daytime sinks
340 of HCHO ultimately produce hydroperoxy (HO_2) radicals. As reported in previous studies, HCHO represents an important source of HO_2 radicals in the atmosphere (Mahajan et al., 2010; Tan et al., 2019a, b).

$$HCHO + OH + O_2 \rightarrow CO + HO_2 + H_2O \tag{R1}$$

$$HCHO + h\nu \rightarrow CO + H_2 \tag{R2}$$

$$HCHO + h\nu + 2O_2 \rightarrow CO + 2HO_2 \tag{R3}$$
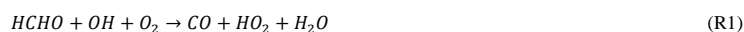
345 Compared with daytime, photolysis frequencies and OH radical concentrations at night are really low so that oxidation of HCHO by OH radicals and photolysis are ineffective sinks. Instead, HCHO dry deposition become the most important nocturnal removal process at night, which depends on both its loss at a surface (described by a surface resistance) and transport to the surface (Fischer et al., 2019; Nussbaumer et al., 2021; Choi et al., 2010; Nguyen et al., 2015; Sumner et al., 2001; Anderson et al., 2017). The HCHO deposition velocity v_d can be estimated from its nighttime concentration decrease
350 (Nussbaumer et al., 2021; Fischer et al., 2019). An average loss rate constant k_d was determined from the HCHO concentration decline from 21:00-01:00 LT divided by the average HCHO concentration during this time interval according to Eq. (7).

$$k_d(HCHO) = \frac{\frac{d[HCHO]}{dt}}{[HCHO]_{av}} \qquad (7)$$

Then the HCHO deposition velocity could be calculated by Eq. (8).

$$v_d(HCHO) = \frac{k_d \times BLH}{x} \qquad (8)$$

355 where BLH denotes the boundary layer height. To consider the inconsistent mixing of the boundary layer at night, the factor x is equal to 2, assuming a linear increase in the HCHO mixing ratio with height in the nocturnal boundary layer (Shepson et al., 1992). During the day, x is set to be 1 for a boundary layer that is well mixed (Fischer et al., 2019; Nussbaumer et al., 2021). Note that this estimation of the dry deposition loss is a lower limit, since it neglects nighttime production of HCHO due to ozonolysis of alkenes, as well as thermally driven turbulence and deposition caused by stomatal uptake by vegetation

360 (Fischer et al., 2019; Nguyen et al., 2015). Figure S4 shows an example of one of the evenings during which HCHO decay followed an apparent first-order kinetics. We have performed this calculation for 9 nights when the estimated HCHO production from ozonolysis of alkenes was around 15% of the observed HCHO loss on average, and an overview of the 9 nights can be found in Figure S5. We finally estimated v_d (night) = 0.52 cm s^{-1} and v_d (day) = 1.04 cm s^{-1}. Table 2 compares dry deposition rates of HCHO reported in previous studies to our estimates, which turn out to be quite similar (DiGangi et al.,

365 2011; Ayers et al., 1997; Stickler et al., 2007; Nussbaumer et al., 2021; Sumner et al., 2001; Choi et al., 2010).

By our estimation, the role of NO$_3$ radicals in HCHO removal at the DSL site was negligible (Sect. S3). Therefore, calculation of the HCHO loss could be expressed as Eq. (9).

$$L(HCHO) = L_{HCHO+OH} + L_{HCHO+h\nu} + L_{deposition}$$

$$= [HCHO] \times ([OH] \times k_{HCHO+OH} + (J(HCHO\_M) + J(HCHO\_R)) + \frac{v_d(HCHO)}{BLH}) \qquad (9)$$

370 The profile of the calculated HCHO loss rates during the campaign is shown in Figure S6, with an average loss rate of 0.49 ppbv h^{-1}. Comparison of HCHO loss rates between the sunny period and the cloudy and rainy period is shown in Table 1.

In Figure 9, the diurnal average HCHO loss rates in both the sunny period and the cloudy and rainy period showed significant diurnal cycles. Daily average loss rates of dry deposition did not show obvious diurnal cycle, which remained relatively constant ranging from 0.08 ppbv h^{-1} to 0.40 ppbv h^{-1} in the sunny period and 0.04 ppbv h^{-1} to 0.12 ppbv h^{-1} in the cloudy and

375 rainy period, owning to co-variation of the concertation of HCHO and BLH. During nighttime in both periods, HCHO loss rates were dominated by dry deposition, when the contributions of photolysis and reactions with OH were so small that they could be neglected. After sunrise, loss rates of photolysis and the reaction with OH radicals began to rise, and reached the maximum at noon. The diurnal maximum loss rates in the sunny period was 2.75 ppbv h^{-1}, about 3 times larger than that in the cloudy and rainy period (0.66 ppbv h^{-1}), both of which occurred at 13:00 LT. After the peak, loss rates of photolysis and the

380 reaction with OH in both ~~phases~~ periods continued to fall and remained low at night. The diurnal average loss rates of HCHO

were 0.78 ppbv h[-1] and 0.22 ppbv h[-1] for the sunny period and the cloudy and rainy period, respectively. Dry deposition played a more important role in HCHO loss in the cloudy and rainy period, accounting for 34.1% of the loss of HCHO, whereas photolysis contributed by 32.8% and the reaction with OH radicals contributed by 33.1%. Reaction with OH radicals was the dominant contributor to HCHO loss in the sunny period, which represented 42.2% of the total HCHO loss, followed by

385 photolysis (39.2%), and dry deposition (18.6%).

The total uncertainties of HCHO loss rates resulted from the uncertainties in the reaction rate coefficients for VOCs and OH radicals, measurements of HCHO, photolysis frequencies, and BLH, and estimations of OH (Table S7), were 28.9% in both the sunny period and the cloudy and rainy period.

3.4 HCHO net production

390 We investigated the daily profiles of hourly averages of HCHO production and loss rates throughout the campaign. Net production of HCHO can be calculated as Eq. (10).

$$Net(HCHO) = P(HCHO) - L(HCHO) \qquad (10)$$

Uncertainties of the calculated net HCHO production rates and the observed rates of HCHO concentration change ($\frac{d[HCHO]}{dt}$) are listed in Table S8. The uncertainty of the observed rates of HCHO concentration change is composed of the HCHO

395 measurement uncertainty and the uncertainty of the fit (30% upper limit) (Nussbaumer et al., 2021) with the latter dominating. Any discrepancy between the calculated net HCHO production rates and the observed rates of HCHO concentration change will be due to either unconsidered chemical terms or meteorological effects (Sumner et al., 2001). Figure 10a shows that our calculated net HCHO production rates are in relatively good agreements with the observed rates of HCHO concentration change throughout the day in the sunny period, indicating that our treatment of chemical terms is accurate, and that HCHO

400 was dominantly secondarily produced at the DSL site, which can be approximated by oxidation of the 24 hydrocarbons we considered in our calculation. Thus, transport processes and primary emissions did not significantly impact ambient HCHO concentrations at the DSL site, at least their influences were considerably tiny compared to the chemical production. During nighttime, the rates of HCHO concentration change oscillated around zero, when the calculated production almost completely balanced the loss term. After 7:00 LT, HCHO production exceeded its loss, leading to positive net HCHO production values,

405 which is in line with the increasing trend of the HCHO concentration. After 15:00 LT, HCHO loss began to transcend its production, resulting in the decline of HCHO abundance. Uncertainties of the calculated net HCHO production rates (38.8%) and the observed rates of HCHO concentration change (30%) led to overlapped uncertainty ranges, as shown in Figure 10a. Thus, the calculated net HCHO production rates are very close to the observed rates of HCHO concentration change. However, during 12:00-14:00 LT, the calculated net HCHO production rates were slightly higher than the observed rates of HCHO

410 concentration change by around 0.6 ppbv h^{-1}, indicating a missing loss term, most likely due to dilution with HCHO-poor air from the nocturnal residual layer, which coincided with the obvious enhancements of the boundary layer height that were usually observed during 11:00-14:00 LT at the DSL site, as shown in Figure S7a.

On the other hand, in the cloudy and rainy days, the observed HCHO concentration remained relatively steady while calculated HCHO production prevailed over its loss, leading to a net production of about 1 ppbv h^{-1} during 8:00-13:00 LT, as

415 shown in Figure 10b. The differences between the calculated net production rates and the observed rates of HCHO concentration change suggest either a missing loss term or an overestimated production. Since differences were still observed from 8:00-13:00 LT in Figure 10b even when uncertainties of the calculated net HCHO production rates (35.7%) and the observed rates of HCHO concentration change (30%) were considered, a real missing loss term was more likely there. Dilution with HCHO-poor air from the nocturnal residual layer due to the increases in the boundary layer height, as we have discussed

420 for the case in the sunny period, might have contributed to the missing loss term, but probably were not the only donor, since the discrepancies found in 12:00-14:00 LT in the sunny days were only half of those found in the cloudy and rainy days, whereas the increases in the boundary layer height in the cloudy and rainy days were smaller compared to those in the sunny days, as shown in Figure S7b. Also, the wind speeds were usually between 1-3 m s^{-1}, which indicates that transport effects from areas with lower HCHO concentrations might not be important. There was significantly more rainfall at daytime in the

425 cloudy and rainy days than in the sunny days during our campaign, and thus we consider the other missing loss process might be wet deposition, which has been reported as a dominant one of the total deposition (i.e. dry deposition and wet deposition) during the rainy season (Seyfioglu et al., 2006). Indeed, HCHO is readily soluble in cloud and rainwater with its high Henry's law constant ($\sim 5.5 \times 10^3$ M atm^{-1}) and could be efficiently converted to formic acid in warm cloud droplets (Allou et al., 2011; Chebbi & Carlier, 1996; Franco et al., 2021). Unfortunately, we did not collect rain samples during our campaign so that we

430 do not have an access to further evaluate this assumption.

4 Conclusions

In this study, ambient HCHO measurements, together with a number of VOC species, were conducted from June 10 to July 4 in 2021 at the DSL site in Shanghai. During the campaign, the average HCHO concentration was 2.2 $\pm$ 1.8 ppbv. The good correlation of HCHO and O$_3$ (R^2=0.73) and the two methods on estimating the contributions of different HCHO sources (i.e.,

435 ratios of HCHO/C$_2$H$_2$ and a multi-linear regression method based on ambient measurements on HCHO, C$_2$H$_2$, and O$_3$) both indicate that secondary sources played an important role in the local HCHO formation. 24 VOC species were considered in the calculation of secondary HCHO production, which shows that the dominant HCHO precursors were isoprene, ethene, methane and propene. In the sunny period, isoprene oxidation by OH radicals contributed the most, whereas reactions of ethene

with OH radicals became the most important path to the HCHO production in the cloudy and rainy period. The diurnal average

440 secondary HCHO production rates were 0.97 and 0.51 ppbv h^{-1} for the sunny period and the cloudy and rainy period, respectively. For the HCHO loss estimation, HCHO photolysis, reactions with OH radicals, and dry deposition, were considered, where loss rates due to photolysis and reactions of OH radicals were significantly larger than that of dry deposition in the sunny period, but these three terms were nearly equivalent in the cloudy and rainy period. The diurnal average loss rates of HCHO were 0.78 ppbv h^{-1} and 0.22 ppbv h^{-1} for the sunny period and the cloudy and rainy period, respectively. The

445 calculated net HCHO production rates were in good agreements with the observed rates of HCHO concentration change throughout the sunny days, indicating that HCHO was approximately produced by oxidation of the 24 VOC species we considered at the DSL site during the campaign.

In summary, our results reveal the important role of secondary formation of HCHO at the suburb of Shanghai, where alkenes are likely the key precursors for HCHO. We provide a HCHO budget based on a comprehensive observation of HCHO

450 precursors, which has rarely been conducted in previous studies. Meanwhile, we found evidences for missing loss processes of HCHO in the cloudy and rainy days, which might be attributed to the HCHO wet deposition, and this may be an important loss term in rainy days and should be further investigated.

Data availability. The data used to support the conclusions in this study are available at a public data repository of Figshare

455 via https://doi.org/10.6084/m9.figshare.20218133.v3 (Wu et al., 2023)

Author contributions. LW designed the study. YZW, JH, GY, YWW, SW, and QF conducted the field campaign. YZW, GY, YWW, and LHW carried out laboratory experiments. JH, SW, QF, and YL provided technical support. YZW analysed the data. YZW and LW wrote the paper with contributions from all of the other co-authors.

460

Competing interest. The authors declare that they have no conflicts of interest.

Acknowledgements. This research was supported by the National Natural Science Foundation of China (21925601, 92044301, 92143301 and 22127811), and Shanghai Municipal Bureau of Ecology and Environment (2021-29).

465

带格式的: 字体颜色: 自动设置

References

Allou, L., El Maimouni, L., and Le Calvé, S.: Henry's law constant measurements for formaldehyde and benzaldehyde as a function of temperature and water composition, Atmos. Environ., 45, 2991–2998, https://doi.org/https://doi.org/10.1016/j.atmosenv.2010.05.044, 2011.

470 Anderson, D. C., Nicely, J. M., Wolfe, G. M., Hanisco, T. F., Salawitch, R. J., Canty, T. P., Dickerson, R. R., Apel, E. C., Baidar, S., Bannan, T. J., Blake, N. J., Chen, D., Dix, B., Fernandez, R. P., Hall, S. R., Hornbrook, R. S., Gregory Huey, L., Josse, B., Jöckel, P., Kinnison, D. E., Koenig, T. K., Le Breton, M., Marécal, V., Morgenstern, O., Oman, L. D., Pan, L. L., Percival, C., Plummer, D., Revell, L. E., Rozanov, E., Saiz-Lopez, A., Stenke, A., Sudo, K., Tilmes, S., Ullmann, K., Volkamer, R., Weinheimer, A. J., Zeng, G., Huey, L. G., Josse, B., Joeckel, P., Kinnison, D. E., Koenig, T. K., Le

475 Breton, M., Marecal, V., Morgenstern, O., Oman, L. D., Pan, L. L., Percival, C., Plummer, D., Revell, L. E., Rozanov, E., Saiz-Lopez, A., Stenke, A., Sudo, K., Tilmes, S., Ullmann, K., Volkamer, R., Weinheimer, A. J., and Zeng, G.: Formaldehyde in the Tropical Western Pacific: Chemical Sources and Sinks, Convective Transport, and Representation in CAM-Chem and the CCMI Models, J. Geophys. Res. Atmos., 122, 11201–11226, https://doi.org/10.1002/2016JD026121, 2017.

480 Ayers, G. P., Gillett, R. W., Granek, H., De Serves, C., and Cox, R. A.: Formaldehyde production in clean marine air, Geophys. Res. Lett., 24, 401–404, https://doi.org/10.1029/97GL00123, 1997.

Chebbi, A. and Carlier, P.: Carboxylic acids in the troposphere, occurrence, sources, and sinks: A review, Atmos. Environ., 30, 4233–4249, https://doi.org/10.1016/1352-2310(96)00102-1, 1996.

Chen, W. T., Shao, M., Lu, S. H., Wang, M., Zeng, L. M., Yuan, B., and Liu, Y.: Understanding primary and secondary sources

485 of ambient carbonyl compounds in Beijing using the PMF model, Atmos. Chem. Phys., 14, 3047–3062, https://doi.org/10.5194/acp-14-3047-2014, 2014.

Choi, W., Faloona, I. C., Bouvier-Brown, N. C., McKay, M., Goldstein, A. H., Mao, J., Brune, W. H., LaFranchi, B. W., Cohen, R. C., Wolfe, G. M., Thornton, J. A., Sonnenfroh, D. M., and Millet, D. B.: Observations of elevated formaldehyde over a forest canopy suggest missing sources from rapid oxidation of arboreal hydrocarbons, Atmos. Chem. Phys., 10,

490 8761–8781, https://doi.org/10.5194/acp-10-8761-2010, 2010.

Claflin, M., Pagonis, D., Finewax, Z., Handschy, A., Day, D., Brown, W., Jayne, J., Worsnop, D., Jimenez, J., Ziemann, P., de Gouw, J., and Lerner, B.: An in situ gas chromatograph with automatic detector switching between PTR- and EI-TOF-MS: isomer-resolved measurements of indoor air, Atmos. Meas. Tech., 14, 133–152, 2021.

DiGangi, J. P., Boyle, E. S., Karl, T., Harley, P., Turnipseed, A., Kim, S., Cantrell, C., Maudlin III, R. L., Zheng, W., Flocke,

495 F., Hall, S. R., Ullmann, K., Nakashima, Y., Paul, J. B., Wolfe, G. M., Desai, A. R., Kajii, Y., Guenther, A., Keutsch, F. N., Maudlin III, R. L., Zheng, W., Flocke, F., Hall, S. R., Ullmann, K., Nakashima, Y., Paul, J. B., Wolfe, G. M., Desai, A. R., Kajii, Y., Guenther, A., and Keutsch, F. N.: First direct measurements of formaldehyde flux via eddy covariance: implications for missing in-canopy formaldehyde sources, Atmos. Chem. Phys., 11, 10565–10578, https://doi.org/10.5194/acp-11-10565-2011, 2011.

500 Dovrou, E., Bates, K. H., Moch, J. M., Mickley, L. J., Jacob, D. J., and Keutsch, F. N.: Catalytic role of formaldehyde in particulate matter formation, Proc. Natl. Acad. Sci. U. S. A., 119, https://doi.org/10.1073/pnas.2113265119, 2022.

Dutta, C., Chatterjee, A., Jana, T. K., Mukherjee, A. K., and Sen, S.: Contribution from the primary and secondary sources to the atmospheric formaldehyde in Kolkata, India, Sci. Total Environ., 408, 4744–4748, https://doi.org/10.1016/j.scitotenv.2010.01.031, 2010.

505 Ehhalt, D. H. and Rohrer, F.: Dependence of the OH concentration on solar UV, J. Geophys. Res. Atmos., 105, 3565–3571, https://doi.org/10.1029/1999JD901070, 2000.

Fan, X., Cai, J., Yan, C., Zhao, J., Guo, Y., Li, C., Dällenbach, K. R., Zheng, F., Lin, Z., Chu, B., Wang, Y., Dada, L., Zha, Q., Du, W., Kontkanen, J., Kurtén, T., Iyer, S., Kujansuu, J. T., Petäjä, T., Worsnop, D. R., Kerminen, V. M., Liu, Y., Bianchi, F., Tham, Y. J., Yao, L., and Kulmala, M.: Atmospheric gaseous hydrochloric and hydrobromic acid in urban

510   Beijing, China: Detection, source identification and potential atmospheric impacts, Atmos. Chem. Phys., 21, 11437–11452, https://doi.org/10.5194/acp-21-11437-2021, 2021.

Fischer, H., Axinte, R., Bozem, H., Crowley, J. N., Ernest, C., Gilge, S., Hafermann, S., Harder, H., Hens, K., Janssen, R. H. H., Königstedt, R., Kubistin, D., Mallik, C., Martinez, M., Novelli, A., Parchatka, U., Plass-Dülmer, C., Pozzer, A., Regelin, E., Reiffs, A., Schmidt, T., Schuladen, J., and Lelieveld, J.: Diurnal variability, photochemical production and
515   loss processes of hydrogen peroxide in the boundary layer over Europe, Atmos. Chem. Phys., 19, 11953–11968, https://doi.org/10.5194/acp-19-11953-2019, 2019.

Franco, B., Blumenstock, T., Cho, C., Clarisse, L., Clerbaux, C., Coheur, P. F., De Mazière, M., De Smedt, I., Dorn, H. P., Emmerichs, T., Fuchs, H., Gkatzelis, G., Griffith, D. W. T., Gromov, S., Hannigan, J. W., Hase, F., Hohaus, T., Jones, N., Kerkweg, A., Kiendler-Scharr, A., Lutsch, E., Mahieu, E., Novelli, A., Ortega, I., Paton-Walsh, C., Pommier, M., Pozzer,
520   A., Reimer, D., Rosanka, S., Sander, R., Schneider, M., Strong, K., Tillmann, R., Van Roozendael, M., Vereecken, L., Vigouroux, C., Wahner, A., and Taraborrelli, D.: Ubiquitous atmospheric production of organic acids mediated by cloud droplets, Nature, 593, 233–237, https://doi.org/10.1038/s41586-021-03462-x, 2021.

Garcia, A. R., Volkamer, R., Molina, L. T., Molina, M. J., Samuelson, J., Mellqvist, J., Galle, B., Herndon, S. C., and Kolb, C. E.: Separation of emitted and photochemical formaldehyde in Mexico City using a statistical analysis and a new pair
525   of gas-phase tracers, Atmos. Chem. Phys., 6, 4545–4557, https://doi.org/10.5194/acp-6-4545-2006, 2006.

Gilman, J. B., Lerner, B. M., Kuster, W. C., and De Gouw, J. A.: Source signature of volatile organic compounds from oil and natural gas operations in northeastern Colorado, Environ. Sci. Technol., 47, 1297–1305, https://doi.org/10.1021/es304119a, 2013.

Gong, D., Wang, H., Zhang, S., Wang, Y., Chen Liu, S., Guo, H., Shao, M., He, C., Chen, D., He, L., Zhou, L., Morawska, L.,
530   Zhang, Y., and Wang, B.: Low-level summertime isoprene observed at a forested mountaintop site in southern China: Implications for strong regional atmospheric oxidative capacity, Atmos. Chem. Phys., 18, 14417–14432, https://doi.org/10.5194/acp-18-14417-2018, 2018.

de Gouw, J. A., Middlebrook, A. M., Warneke, C., Goldan, P. D., Kuster, W. C., Roberts, J. M., Fehsenfeld, F. C., Worsnop, D. R., Canagaratna, M. R., Pszenny, A. A. P., Keene, W. C., Marchewka, M., Bertman, S. B., and Bates, T. S.: Budget of
535   organic carbon in a polluted atmosphere: Results from the New England Air Quality Study in 2002, J. Geophys. Res. Atmos., 110, 1–22, https://doi.org/10.1029/2004JD005623, 2005.

de Gouw, J. A., Gilman, J. B., Kim, S. W., Alvarez, S. L., Dusanter, S., Graus, M., Griffith, S. M., Isaacman-VanWertz, G., Kuster, W. C., Lefer, B. L., Lerner, B. M., McDonald, B. C., Rappenglück, B., Roberts, J. M., Stevens, P. S., Stutz, J., Thalman, R., Veres, P. R., Volkamer, R., Warneke, C., Washenfelder, R. A., and Young, C. J.: Chemistry of Volatile
540   Organic Compounds in the Los Angeles Basin: Formation of Oxygenated Compounds and Determination of Emission Ratios, J. Geophys. Res. Atmos., 123, 2298–2319, https://doi.org/10.1002/2017JD027976, 2018.

Gu, C., Wang, S., Zhu, J., Wu, S., Duan, Y., Gao, S., and Zhou, B.: Investigation on the urban ambient isoprene and its oxidation processes, Atmos. Environ., 270, 118870, https://doi.org/10.1016/j.atmosenv.2021.118870, 2022.

Guo, H., Ling, Z. H., Simpson, I. J., Blake, D. R., and Wang, D. W.: Observations of isoprene, methacrolein (MAC) and
545   methyl vinyl ketone (MVK) at a mountain site in Hong Kong, J. Geophys. Res. Atmos., 117, 1–13, https://doi.org/10.1029/2012JD017750, 2012.

Han, Y., Huang, X., Wang, C., Zhu, B., and He, L.: Characterizing oxygenated volatile organic compounds and their sources in rural atmospheres in China, J. Environ. Sci. (China), 81, 148–155, https://doi.org/10.1016/j.jes.2019.01.017, 2019.

Helmig, D.: Ozone removal techniques in the sampling of atmospheric volatile organic trace gases, Atmos. Environ., 31, 3635–
550   3651, https://doi.org/10.1016/S1352-2310(97)00144-1, 1997.

Ho, K. F., Ho, S. S. H., Huang, R. J., Dai, W. T., Cao, J. J., Tian, L., and Deng, W. J.: Spatiotemporal distribution of carbonyl compounds in China, Environ. Pollut., 197, 316–324, https://doi.org/10.1016/j.envpol.2014.11.014, 2015.

Hong, Q., Zhu, L., Xing, C., Hu, Q., Lin, H., Zhang, C., Zhao, C., Liu, T., Su, W., and Liu, C.: Inferring vertical variability and diurnal evolution of O3 formation sensitivity based on the vertical distribution of summertime HCHO and NO2 in Guangzhou, China., Sci. Total Environ., 827, 154045, https://doi.org/10.1016/j.scitotenv.2022.154045, 2022.

Kumar, V. and Sinha, V.: VOC–OHM: A new technique for rapid measurements of ambient total OH reactivity and volatile organic compounds using a single proton transfer reaction mass spectrometer, Int. J. Mass Spectrom., 374, 55–63, https://doi.org/https://doi.org/10.1016/j.ijms.2014.10.012, 2014.

Lee, Y. N., Zhou, X., Kleinman, L. I., Nunnermacker, L. J., Springston, S. R., Daum, P. H., Newman, L., Keigley, W. G., Holdren, M. W., Spicer, C. W., Young, V., Fu, B., Parrish, D. D., Holloway, J., Williams, J., Roberts, J. M., Ryerson, T. B., and Fehsenfeld, F. C.: Atmospheric chemistry and distribution of formaldehyde and several multioxygenated carbonyl compounds during the 1995 Nashville/Middle Tennessee Ozone Study, J. Geophys. Res. Atmos., 103, 22449–22462, https://doi.org/10.1029/98JD01251, 1998.

Li, J., Xie, S. D., Zeng, L. M., Li, L. Y., Li, Y. Q., and Wu, R. R.: Characterization of ambient volatile organic compounds and their sources in Beijing, before, during, and after Asia-Pacific Economic Cooperation China 2014, Atmos. Chem. Phys., 15, 7945–7959, https://doi.org/10.5194/acp-15-7945-2015, 2015.

Lin, Y. C., Schwab, J. J., Demerjian, K. L., Bae, M.-S. S., Chen, W.-N. N., Sun, Y., Zhang, Q., Hung, H.-M. M., and Perry, J.: Summertime formaldehyde observations in New York City: Ambient levels, sources and its contribution to HOx radicals, J. Geophys. Res. Atmos., 117, 1–14, https://doi.org/10.1029/2011JD016504, 2012.

Liu, L., Flatoy, F., Ordonez, C., Braathen, G. O., Hak, C., Junkermann, W., Andreani-Aksoyoglu, S., Mellqvist, J., Galle, B., Prevot, A. S. H., and Isaksen, I. S. A.: Photochemical modelling in the Po basin with focus on formaldehyde and ozone, Atmosphecic Chem. Phys., 7, 121–137, https://doi.org/10.5194/acp-7-121-2007, 2007.

Liu, Y., Zhang, Y., Lian, C., Yan, C., Feng, Z., Zheng, F., Fan, X., Chen, Y., Wang, W., Chu, B., Wang, Y., Cai, J., Du, W., R. Daellenbach, K., Kangasluoma, J., Bianchi, F., Kujansuu, J., Petäjä, T., Wang, X., Hu, B., Wang, Y., Ge, M., He, H., and Kulmala, M.: The promotion effect of nitrous acid on aerosol formation in wintertime in Beijing: The possible contribution of traffic-related emissions, Atmos. Chem. Phys., 20, 13023–13040, https://doi.org/10.5194/acp-20-13023-2020, 2020.

Mahajan, A. S., Whalley, L. K., Kozlova, E., Oetjen, H., Mendez, L., Furneaux, K. L., Goddard, A., Heard, D. E., Plane, J. M. C., and Saiz-Lopez, A.: DOAS observations of formaldehyde and its impact on the HOx balance in the tropical Atlantic marine boundary layer, J. Atmos. Chem., 66, 167–178, https://doi.org/10.1007/s10874-011-9200-7, 2010.

Nguyen, T. B., Crounse, J. D., Teng, A. P., Clair, J. M. S., Paulot, F., Wolfe, G. M., and Wennberg, P. O.: Rapid deposition of oxidized biogenic compounds to a temperate forest, Proc. Natl. Acad. Sci. U. S. A., 112, E392–E401, https://doi.org/10.1073/pnas.1418702112, 2015.

Nussbaumer, C. M., Crowley, J. N., Schuladen, J., Williams, J., Hafermann, S., Reiffs, A., Axinte, R., Harder, H., Ernest, C., Novelli, A., Sala, K., Martinez, M., Mallik, C., Tomsche, L., Plass-Dülmer, C., Bohn, B., Lelieveld, J., Fischer, H., Plass-Dulmer, C., Bohn, B., Lelieveld, J., and Fischer, H.: Measurement report: Photochemical production and loss rates of formaldehyde and ozone across Europe, Atmos. Chem. Phys., 21, 18413–18432, https://doi.org/10.5194/acp-2021-694, 2021.

Obersteiner, F., Bönisch, H., and Engel, A.: An automated gas chromatography time-of-flight mass spectrometry instrument for the quantitative analysis of halocarbons in air, Atmos. Meas. Tech., 9, 179–194, https://doi.org/10.5194/amt-9-179-2016, 2016.

Pavel, M. R. S., Zaman, S. U., Jeba, F., and Salam, A.: Long-Term (2011-2019) Trends of O3, NO2, and HCHO and Sensitivity Analysis of O3 Chemistry over the GBM (Ganges-Brahmaputra-Meghna) Delta: Spatial and Temporal Variabilities, ACS Earth Sp. Chem., 5, 1468–1485, https://doi.org/10.1021/acsearthspacechem.1c00057, 2021.

Possanzini, M., Di Palo, V., and Cecinato, A.: Sources and photodecomposition of formaldehyde and acetaldehyde in Rome ambient air, Atmos. Environ., 36, 3195–3201, https://doi.org/10.1016/S1352-2310(02)00192-9, 2002.

Rohrer, F. and Berresheim, H.: Strong correlation between levels of tropospheric hydroxyl radicals and solar ultraviolet radiation, Nature, 442, 184–187, https://doi.org/10.1038/nature04924, 2006.

Seyfioglu, R., Odabasi, M., and Cetin, E.: Wet and dry deposition of formaldehyde in Izmir, Turkey, Sci. Total Environ., 366, 809–818, https://doi.org/10.1016/j.scitotenv.2005.08.005, 2006.

Shepson, P. B., Bottenheim, J. W., and Hastie, D. R.: Determination of the relative ozone and PAN deposition velocities at night, Geophys. Res. Lett., 19, 1121–1124, 1992.

Stickler, A., Fischer, H., Bozem, H., Gurk, C., Schiller, C., Martinez-Harder, M., Kubistin, D., Harder, H., Williams, J., Eerdekens, G., Yassaa, N., Ganzeveld, L., Sander, R., and Lelieveld, J.: Chemistry, transport and dry deposition of trace gases in the boundary layer over the tropical Atlantic Ocean and the Guyanas during the GABRIEL field campaign, Atmos. Chem. Phys., 7, 3933–3956, https://doi.org/10.5194/acp-7-3933-2007, 2007.

Su, W., Liu, C., Hu, Q., Zhao, S., Sun, Y., Wang, W., Zhu, Y., Liu, J., and Kim, J.: Primary and secondary sources of ambient formaldehyde in the Yangtze River Delta based on Ozone Mapping and Profiler Suite (OMPS) observations, Atmos. Chem. Phys., 19, 6717–6736, https://doi.org/10.5194/acp-19-6717-2019, 2019.

Sumner, A. L., Shepson, P. B., Couch, T. L., Thornberry, T., Carroll, M. A., Sillman, S., Pippin, M., Bertman, S., Tan, D., Faloona, I., Brune, W., Young, V., Cooper, O., Moody, J., and Stockwell, W.: A study of formaldehyde chemistry above a forest canopy, J. Geophys. Res. Atmos., 106, 24387–24405, https://doi.org/10.1029/2000JD900761, 2001.

Sun, Y., Yin, H., Liu, C., Zhang, L., Cheng, Y., Palm, M., Notholt, J., Lu, X., Vigouroux, C., Zheng, B., Wang, W., Jones, N., Shan, C., Qin, M., Tian, Y., Hu, Q., Meng, F., and Liu, J.: Mapping the drivers of formaldehyde (HCHO) variability from 2015 to 2019 over eastern China: insights from Fourier transform infrared observation and GEOS-Chem model simulation, Atmos. Chem. Phys., 21, 6365–6387, https://doi.org/10.5194/acp-21-6365-2021, 2021.

Tan, Z., Lu, K., Jiang, M., Su, R., Wang, H., Lou, S., Fu, Q., Zhai, C., Tan, Q., Yue, D., Chen, D., Wang, Z., Xie, S., Zeng, L., and Zhang, Y.: Daytime atmospheric oxidation capacity in four Chinese megacities during the photochemically polluted season: A case study based on box model simulation, Atmos. Chem. Phys., 19, 3493–3513, https://doi.org/10.5194/acp-19-3493-2019, 2019a.

Tan, Z., Lu, K., Hofzumahaus, A., Fuchs, H., Bohn, B., Holland, F., Liu, Y., Rohrer, F., Shao, M., Sun, K., Wu, Y., Zeng, L., Zhang, Y., Zou, Q., Kiendler-Scharr, A., Wahner, A., and Zhang, Y.: Experimental budgets of OH, HO2, and RO2 radicals and implications for ozone formation in the Pearl River Delta in China 2014, Atmos. Chem. Phys., 19, 7129–7150, https://doi.org/10.5194/acp-19-7129-2019, 2019b.

Wang, C., Huang, X.-F. F., Han, Y., Zhu, B., and He, L.-Y. Y.: Sources and Potential Photochemical Roles of Formaldehyde in an Urban Atmosphere in South China, J. Geophys. Res. Atmos., 122, 11934–11947, https://doi.org/10.1002/2017JD027266, 2017.

Wang, X., Wang, H., and Wang, S.: Ambient formaldehyde and its contributing factor to ozone and OH radical in a rural area, Atmos. Environ., 44, 2074–2078, https://doi.org/10.1016/j.atmosenv.2010.03.023, 2010.

Wittrock, F., Richter, A., Oetjen, H., Burrows, J. P., Kanakidou, M., Myriokefalitakis, S., Volkamer, R., Beirle, S., Platt, U., and Wagner, T.: Simultaneous global observations of glyoxal and formaldehyde from space, Geophys. Res. Lett., 33, https://doi.org/10.1029/2006GL026310, 2006.

Wu, Y., Huo, J., Yang, G., Wang, Y., Wang, L., Wu, S., Yao, L., Fu, Q., and Wang, L.: Data for the study for HCHO production and loss rates in a suburban site of Shanghai [Dataset], Figshare, https://doi.org/10.6084/m9.figshare.20218133.v3, 2023.

Xing, C., Liu, C., Hu, Q., Fu, Q., Lin, H., Wang, S., Su, W., Wang, W., Javed, Z., and Liu, J.: Identifying the wintertime sources of volatile organic compounds (VOCs) from MAX-DOAS measured formaldehyde and glyoxal in Chongqing, southwest China, Sci. Total Environ., 715, https://doi.org/10.1016/j.scitotenv.2019.136258, 2020.

Yang, G., Huo, J., Wang, L. L., Wang, Y., Wu, S., Yao, L., Fu, Q., and Wang, L. L.: Total OH Reactivity Measurements in a Suburban Site of Shanghai, J. Geophys. Res. Atmos., 127, e2021JD035981, https://doi.org/https://doi.org/10.1029/2021JD035981, 2022.

Yuan, B., Shao, M., De Gouw, J., Parrish, D. D., Lu, S., Wang, M., Zeng, L., Zhang, Q., Song, Y., Zhang, J., and Hu, M.: Volatile organic compounds (VOCs) in urban air: How chemistry affects the interpretation of positive matrix factorization (PMF) analysis, J. Geophys. Res. Atmos., 117, 1–17, https://doi.org/10.1029/2012JD018236, 2012.

Yuan, B., Hu, W. W., Shao, M., Wang, M., Chen, W. T., Lu, S. H., Zeng, L. M., and Hu, M.: VOC emissions, evolutions and
645   contributions to SOA formation at a receptor site in eastern China, Atmos. Chem. Phys., 13, 8815–8832, https://doi.org/10.5194/acp-13-8815-2013, 2013.

Zhang, H., Li, J., Ying, Q., Guven, B. B., and Olaguer, E. P.: Source apportionment of formaldehyde during TexAQS 2006 using a source-oriented chemical transport model, J. Geophys. Res. Atmos., 118, 1525–1535, https://doi.org/10.1002/jgrd.50197, 2013.

650   Zhang, K., Duan, Y., Huo, J., Huang, L., Wang, Y. Y., Fu, Q., Wang, Y. Y., and Li, L.: Formation mechanism of HCHO pollution in the suburban Yangtze River Delta region, China: A box model study and policy implementations, Atmos. Environ., 267, 118755, https://doi.org/10.1016/j.atmosenv.2021.118755, 2021a.

Zhang, S., Wang, S., Zhang, R., Guo, Y., Yan, Y., Ding, Z., and Zhou, B.: Investigating the Sources of Formaldehyde and Corresponding Photochemical Indications at a Suburb Site in Shanghai From MAX-DOAS Measurements, J. Geophys.
655   Res. Atmos., 126, https://doi.org/10.1029/2020JD033351, 2021b.

Zhang, X., He, S. Z., Chen, Z. M., Zhao, Y., and Hua, W.: Methyl hydroperoxide (CH3OOH) in urban, suburban and rural atmosphere: Ambient concentration, budget, and contribution to the atmospheric oxidizing capacity, Atmos. Chem. Phys., 12, 8951–8962, https://doi.org/10.5194/acp-12-8951-2012, 2012.

Zhou, X., Huang, G., Civerolo, K., Roychowdhury, U., and Demerjian, K. L.: Summertime observations of HONO, HCHO,
660   and O3 at the summit of Whiteface Mountain, New York, J. Geophys. Res. Atmos., 112, 1–13, https://doi.org/10.1029/2006JD007256, 2007.

Zhu, L., Jacob, D. J., Keutsch, F. N., Mickley, L. J., Scheffe, R., Strum, M., Abad, G. G., Chance, K., Yang, K., Rappengluck, B., Millet, D. B., Baasandorj, M., Jaegle, L., and Shah, V.: Formaldehyde (HCHO) As a Hazardous Air Pollutant: Mapping Surface Air Concentrations from Satellite and Inferring Cancer Risks in the United States, Environ. Sci. Technol., 51,
665   5650–5657, https://doi.org/10.1021/acs.est.7b01356, 2017.

Table 1. Comparison of the HCHO concentration, HCHO production rates, and HCHO loss rates between the sunny period and the cloudy and rainy period.

Period	The whole campaign	The sunny period	The cloudy and rainy period
Date	6.10—7.4	6.11, 6.12, 6.15, 6.16, 6.21—6.25, 6.29—7.1	6.10, 6.13, 6.14, 6.17—6.20, 6.26—6.28, 7.2—7.4
Average HCHO concentration (ppbv)	2.2	2.8	1.7
10th percentile of HCHO concentration (ppbv)	0.4	0.3	0.5
90th percentile of HCHO concentration (ppbv)	4.9	6.2	3.4
Average HCHO production rates (ppbv h^{-1})	0.73	0.97	0.51
10th percentile of HCHO production rates (ppbv h^{-1})	0.01	0.01	0.01
90th percentile of HCHO production rates (ppbv h^{-1})	2.42	3.15	1.53
Average HCHO loss rates (ppbv h^{-1})	0.49	0.78	0.22
10th percentile of HCHO loss rates (ppbv h^{-1})	0.02	0.01	0.02
90th percentile of HCHO loss rates (ppbv h^{-1})	1.46	2.64	0.5

670

Table 2. A summary of HCHO deposition velocities.

Site	Time	Daytime dry deposition velocities (cm s^{-1})	Nighttime dry deposition velocities (cm s^{-1})	Reference
Shanghai, China Suburban area	Summer 2021	1.04	0.52	This study
Hohenpeißenberg, Germany Suburban area	Summer 2012	0.94	0.47	(Nussbaumer et al., 2021)
Colorado, America Suburban area	Summer 2010	0.39	0.18	(DiGangi et al., 2011)
California, America Suburban area	Autumn 2007	1.5	0.84	(Choi et al., 2010)
Michigan, America Suburban area	Summer 1998	1.5	0.65	(Sumner et al., 2001)
Cape Grim, Australia Suburban area	Winter 1993	--	0.5	(Ayers et al., 1997)
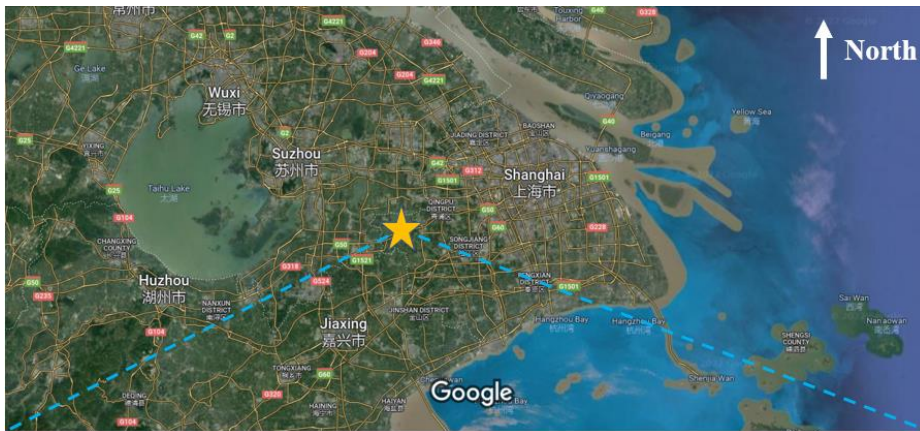
Figure 1. A Topography map (from ©Google Maps) of the region around the Dianshan Lake (DSL) Air Quality Monitoring Supersite (31.10°N, 120.98°E).
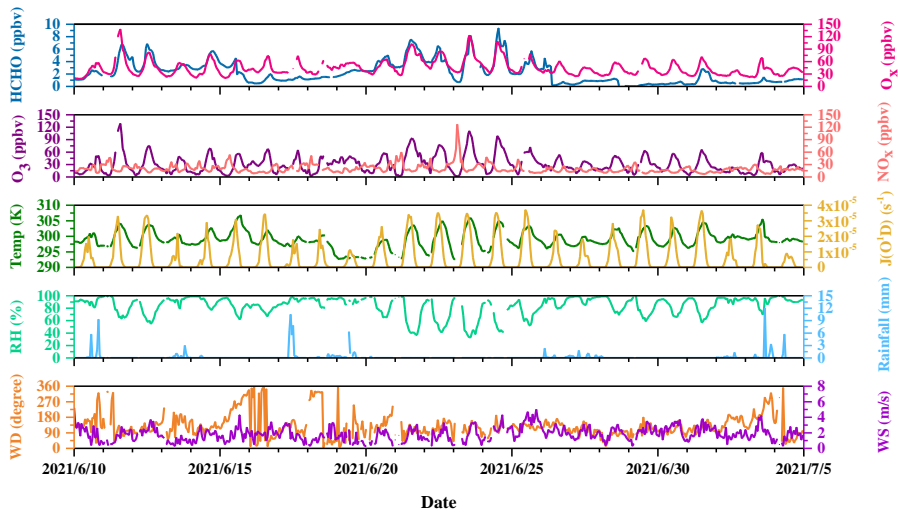
Figure 2. Time profiles of HCHO, O_x (=NO_2+O_3), O_3, NO_x, photolysis frequencies of O^1D ($J(O^1D)$) and meteorological parameters during the campaign.
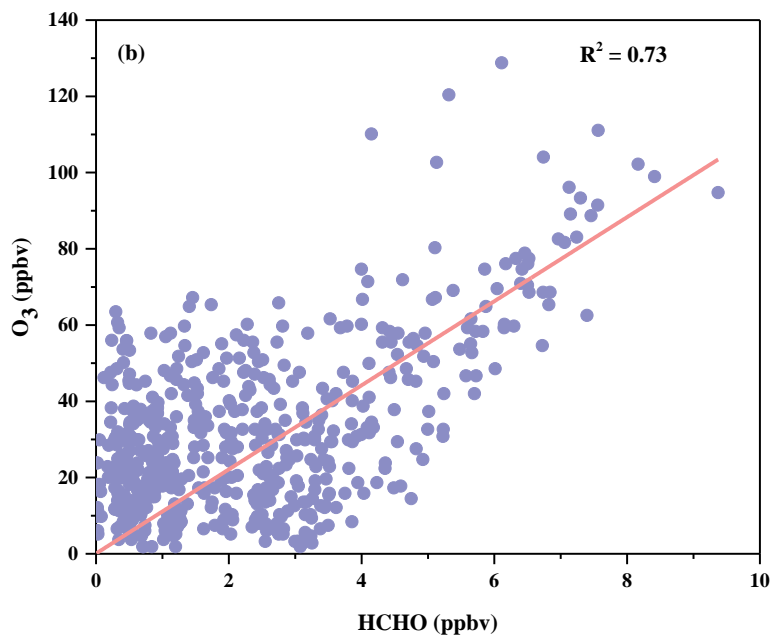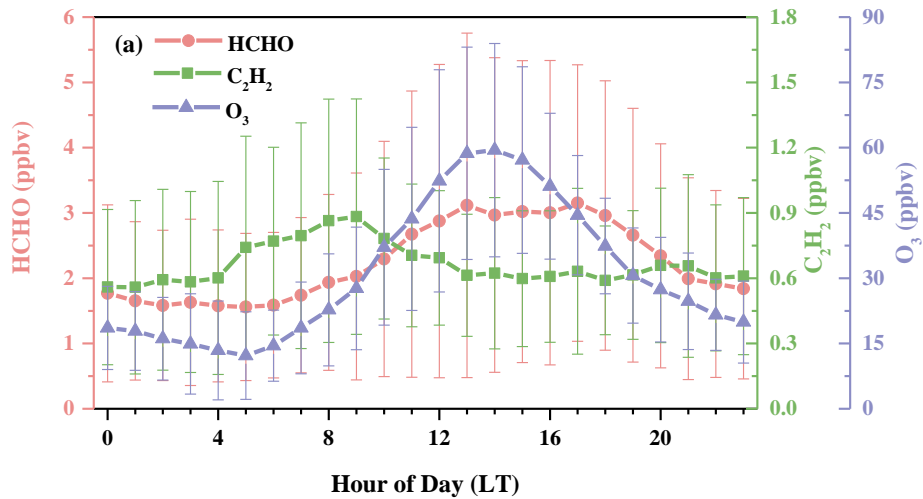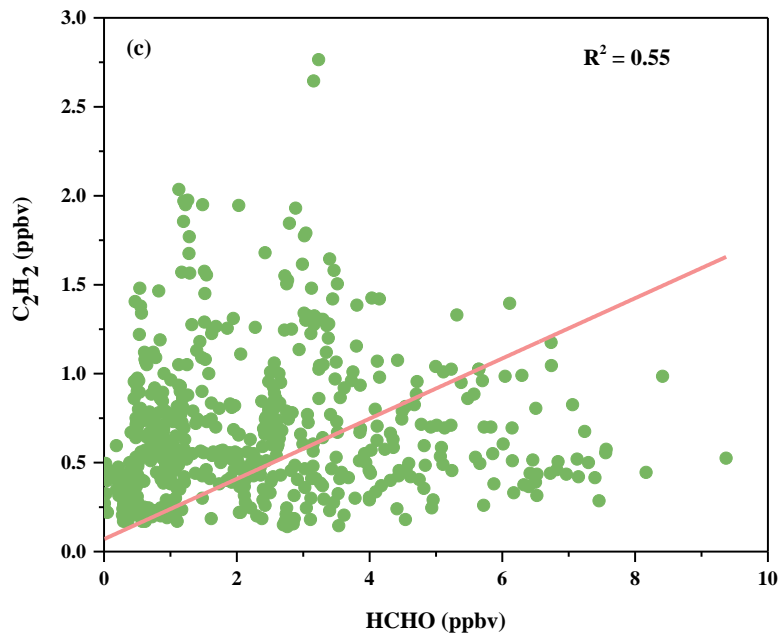
Figure 3. (a) Diurnal patterns of HCHO, O_3, and C_2H_2, with the error bar indicating one standard deviation; (b) Correlation between measured concentrations of HCHO and O_3; (c) Correlation between measured concentrations of HCHO and C_2H_2.

685
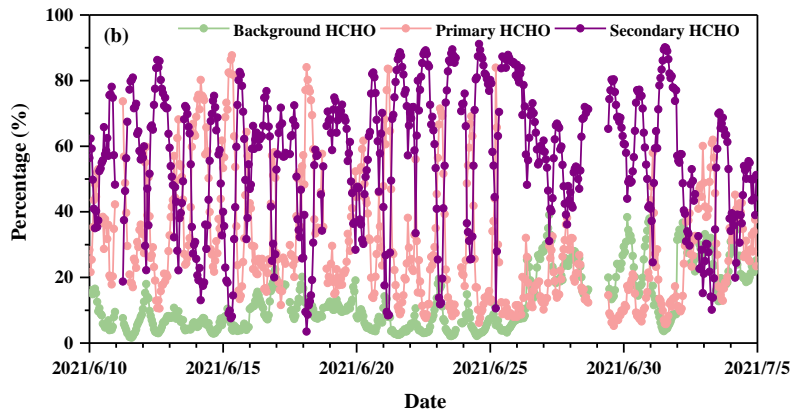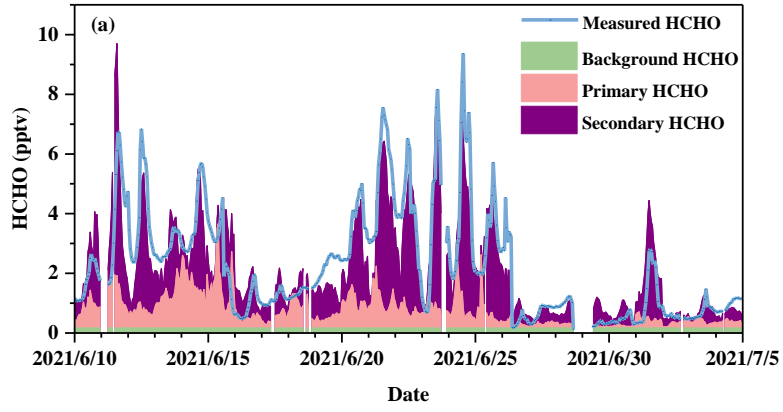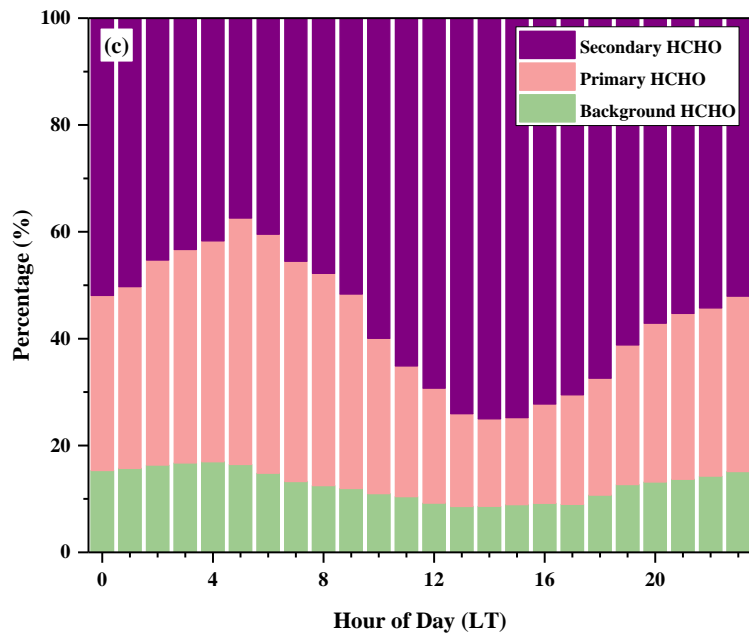
690

Figure 4. (a) Time series and (b) relative contributions of background, primary, and secondary sources to HCHO from a multi-linear regression model during the campaign, and (c) campaign-average diurnal contributions of background, primary, and secondary sources.
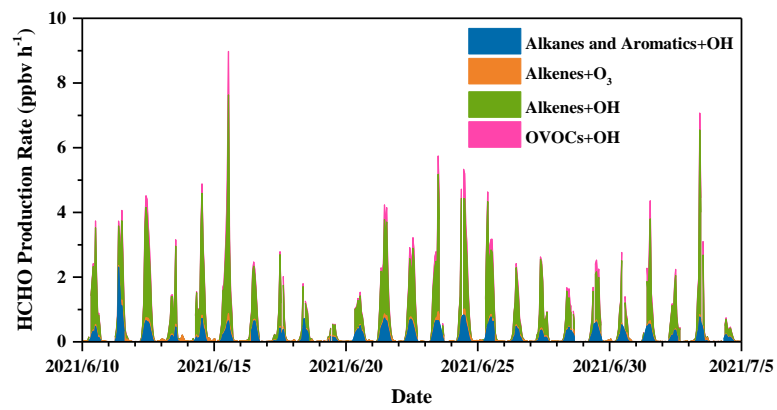
Figure 5. Time profiles of the calculated HCHO production rates during the campaign.

695
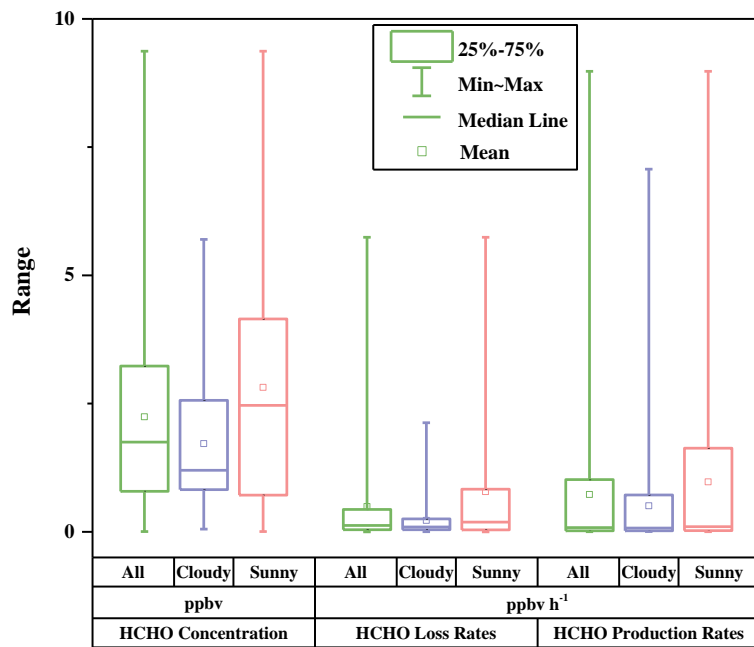
Figure 6. Box plots of HCHO concentration, HCHO loss rates, and HCHO production rates during the whole campaign (All), the cloudy and rainy period (Cloudy), and the sunny period (Sunny). The squares represent the mean, the bands inside the box represent the median, the bottom and top of the box represent the lower and upper quartiles, respectively, and the ends of the whiskers show the min and the max.
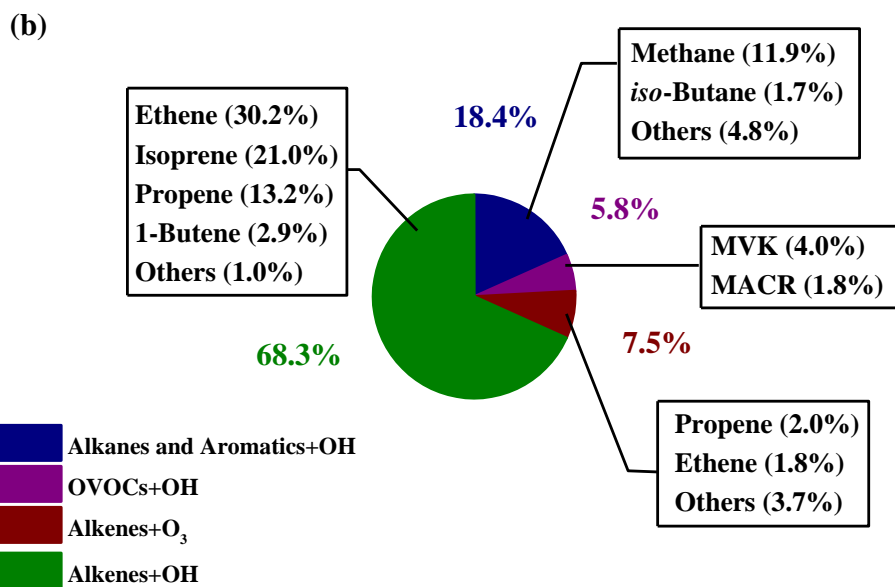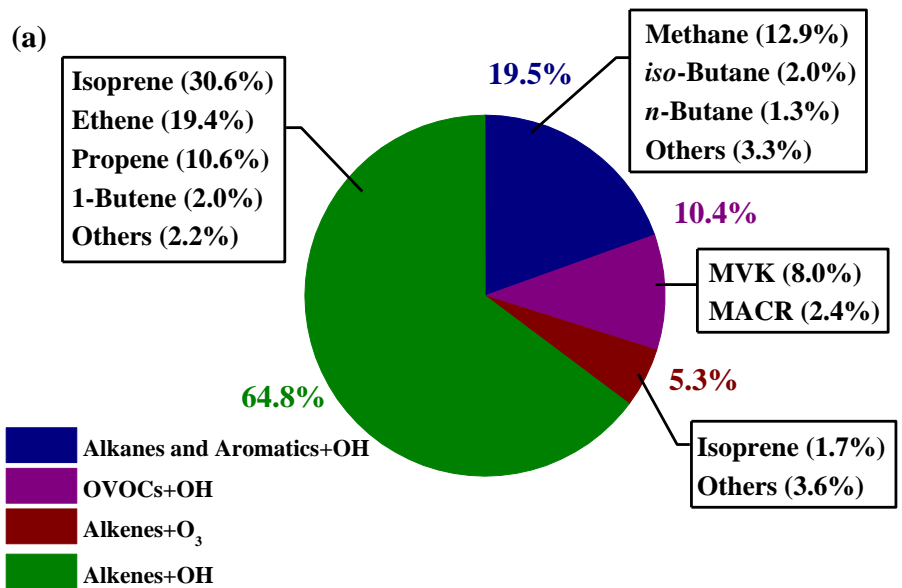
705 **Figure 7**. Relative contributions to HCHO production rates in (a) the sunny period and (b) the cloudy and rainy period. The relative contributions to HCHO production are shown for the top 10 VOC species in each ~~phase~~period. The area of pie charts is in proportion to the calculated HCHO production rates in two periods.
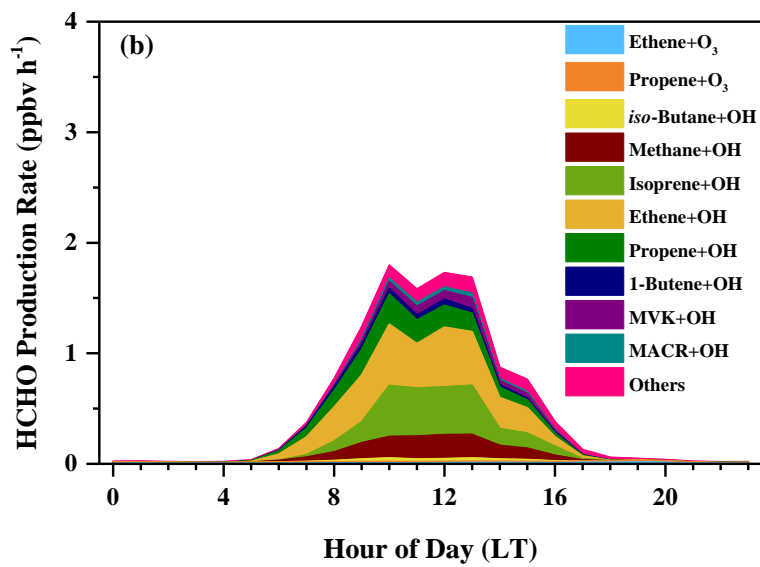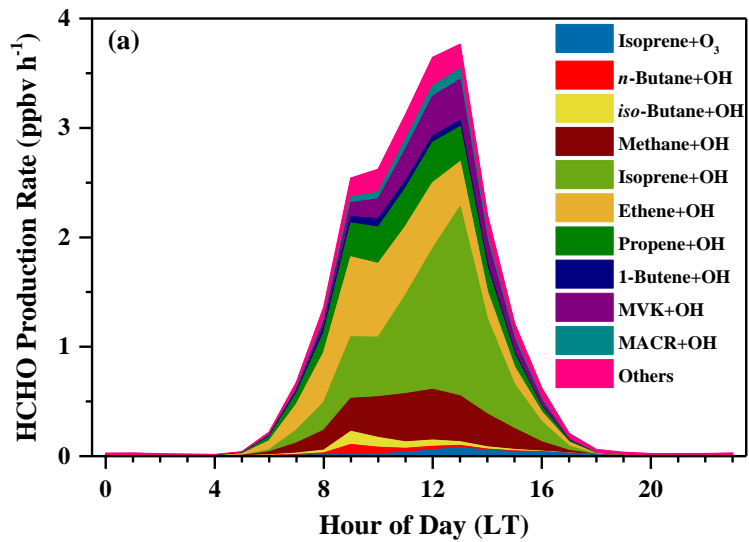
710   **Figure 8**. **Average diurnal variations of HCHO production rates (ppbv h^{-1}) from the OH-initiated and O$_3$-initiated oxidation during (a) the sunny period and (b) the cloudy and rainy period.**
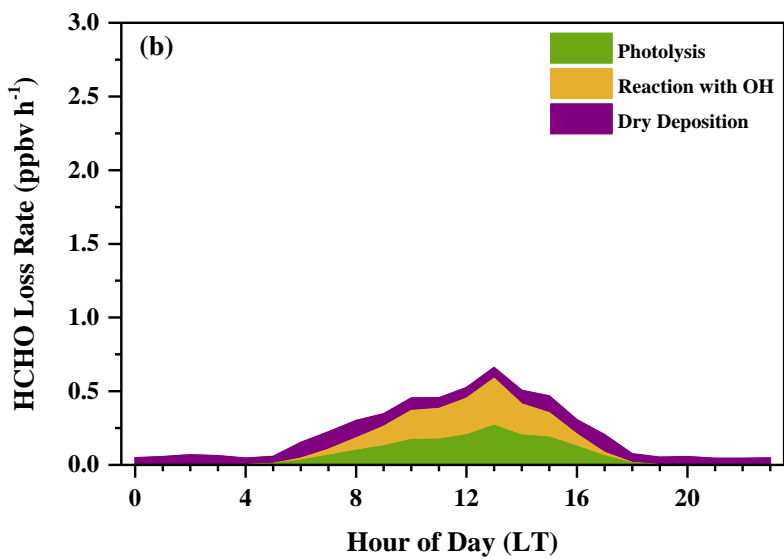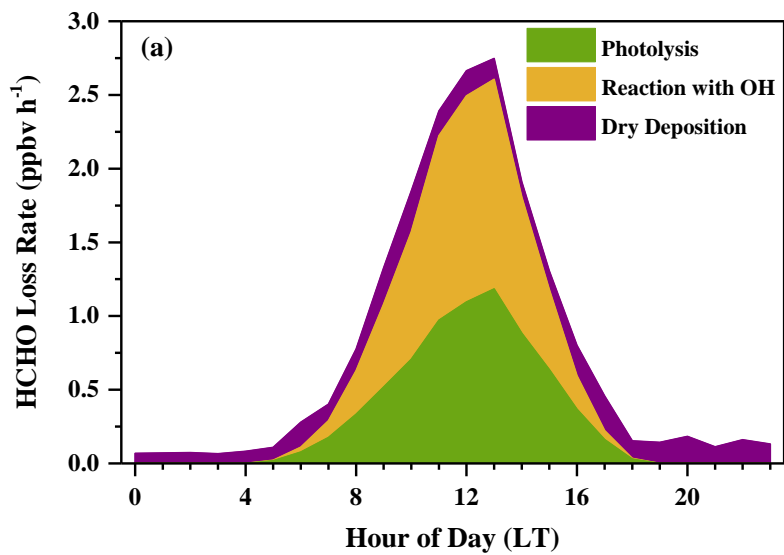
715 **Figure 9**. **Average diurnal variations of HCHO loss rates (ppbv h[-1]) from photolysis, reaction with OH radicals and dry deposition during (a) the sunny period and (b) the cloudy and rainy period.**
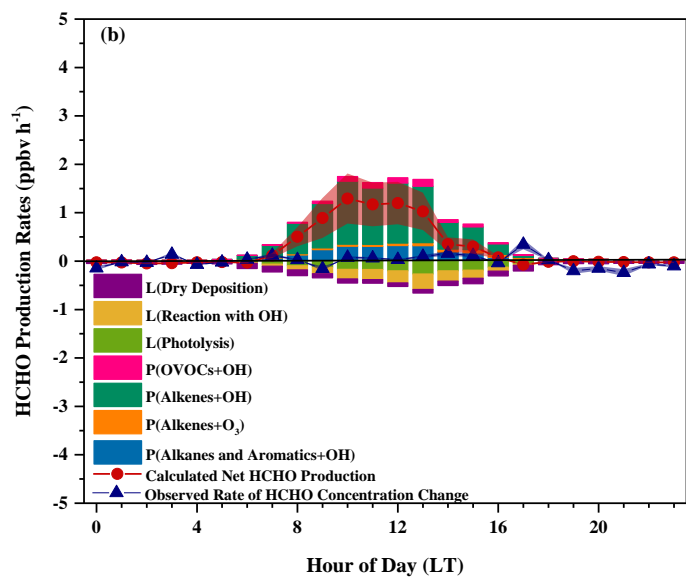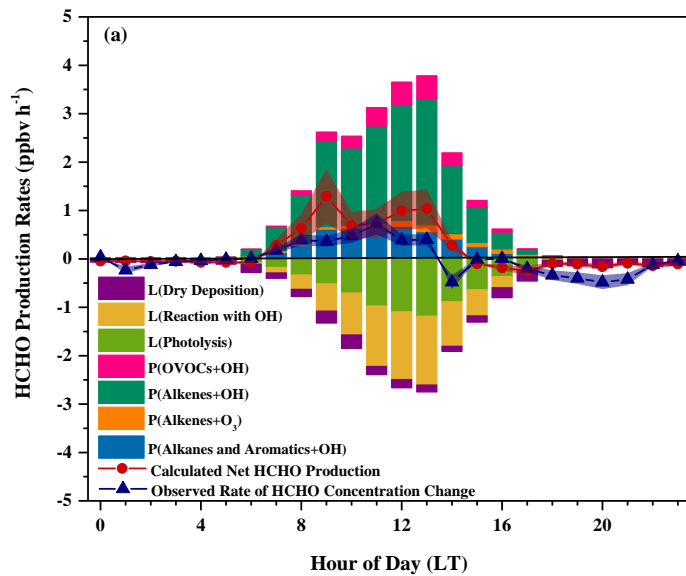
Figure 10. Average daytime production rates, loss rates, the calculated net production rates, and the observed rates of HCHO concentration change for (a) the sunny and (b) the cloudy and rainy period. Shaded areas give the uncertainties of the calculated net production rates and the observed rates of HCHO concentration change.